CrossMark

J. Fluid Mech. (2019), *vol.* 873, *pp.* 72–88. © Cambridge University Press 2019
doi:10.1017/jfm.2019.373

Marangoni circulation by UV light modulation on sessile drop for particle agglomeration

Tianyi Li[1], Aravinda Kar[2] and Ranganathan Kumar[1,†]

[1]Department of Mechanical and Aerospace Engineering, University of Central Florida, Orlando, FL 32816, USA

[2]The College of Optics and Photonics, University of Central Florida, Orlando, FL 32816, USA

(Received 20 December 2018; revised 29 April 2019; accepted 2 May 2019;
first published online 20 June 2019)

An analytical solution of a biharmonic equation is presented in axisymmetric toroidal coordinates for Stokes flow due to surface tension gradient on the free surface of sessile drops. The stream function profiles exhibit clockwise and counter-clockwise toroidal volumes. The ring or dot formed by the downward dividing streamlines between these volumes predicts the experimentally deposited particle ring or dot well. This finding suggests that the downward dividing streamline can be taken to be a reasonable indicator of where deposition occurs. Different light patterns directed at different locations of the droplet can give rise to a single spot or ring. A relationship between the positions of the light intensity peak and possible locations of particle deposition is analysed to demonstrate that the streamlines can be generated on-demand to achieve particle deposition at predetermined locations on the substrate. Toroidal corner vortices called Moffatt eddies have appeared in other corner flows and develop in this optical Marangoni flow as well near the contact line.

Key words: drops, Marangoni convection, suspensions

1. Introduction

Microstructures and nanostructures can be manufactured by depositing particles on a solid surface (Vogel *et al.* 2015). The simplest way to deposit nanoparticles on a substrate is by using controlled evaporation of droplets (Kim *et al.* 2011). By exploiting the capillary force of water, combined with controlled evaporation, a vertical deposition method has also been developed (Armstrong *et al.* 2014). However, due to the number of parameters to be controlled in evaporation methods, external forces have been used for controlling deposition patterns, such as electrostatic deposition (Zhang *et al.* 2010) and electrophoretic deposition (Huang *et al.* 2007). The requirements on hydrophilic or hydrophobic properties of substrates used in direct deposition are considered as being high.

Particle deposition by drying or evaporation has been in vogue for some time. The coffee-ring effect (Deegan *et al.* 1997; Deegan 2000) and related theoretical studies on deposition pattern and control have attracted a great deal of attention in

† Email address for correspondence: Ranganathan.Kumar@ucf.edu

https://doi.org/10.1017/jfm.2019.373 Published online by Cambridge University Press

this field. The competition between pinning and dewetting (Deegan 2000) along with the deposition of colloidal particles in droplets (Fischer 2002) have been reported. Flow fields in droplets under slow evaporation have been solved numerically and lubrication theory has been used for different contact angles (Hu & Larson 2005*a*,*b*). The exact analytical solution for Stokes flow in both inviscid and viscous droplets due to evaporation has also been provided by Masoud & Felske (2009*a*,*b*) who evaluated the stream function and velocities for normal velocity boundary conditions at the free surface in toroidal coordinates. In addition to evaporation, surface tension also affects the flow (Scriven & Sternling 1964) especially in creeping flow (Jeong & Moffatt 1992). Surface tension-induced circulation has also been studied by evaluating solutal Marangoni flow with different solutes (Marin *et al.* 2016; Diddens *et al.* 2017) and by evaluating thermal Marangoni flow experimentally and analytically in spherical drop or spherical cap (Ristenpart *et al.* 2007; Tam *et al.* 2009). In Stokes flows, corner vortices called the Moffatt eddies (Moffatt 1964; Shtern 2018) may appear in succession at a fixed geometric ratio in size and intensity (Shankar 1993; Biswas & Kalita 2018).

Not all direct deposition methods can be arbitrarily applied to any particle which might have unique physical and chemical properties. In order to deposit particles, UV light (365 nm wavelength) may need be passed through the droplet made of photosensitive solution using a novel evaporative optical Marangoni convection (Anyfantakis & Baigl 2014; Varanakkottu *et al.* 2015; Anyfantakis *et al.* 2017). AzoTAB is a type of photosensitive surfactant having two isomers, trans-azoTAB and cis-azoTAB (Brown, Butts & Eastoe 2013). Transition of trans-azoTAB to cis-azoTAB under UV light increases the surface tension of the solution (Chevallier *et al.* 2011). Despite the preponderance of research in particle deposition, no analytical work has been done in an attempt to understand the precise control of deposition using a laser as the source to deposit particles. The optical Marangoni flow method is robust, has the ability to assemble various particles in photosensitive surfactant solutions on different substrates and has shown promise in different fields.

This work provides a theoretical framework in toroidal coordinates following Masoud & Felske (2009*b*) to understand the Marangoni flow patterns in photosensitive droplets for tangential stress as the boundary condition at the free surface of the droplet. This boundary condition arises due to surface tension gradients induced by different UV light intensity patterns. The analytical solution identifies the primary circulation regions and downward dividing streamline locations where the suspended particles are likely to agglomerate. The relationship between the location of particle deposition and the location of UV beam is provided as a guidance for precise control of deposition.

2. Model development and solutions

2.1. *The model and a general solution*

The geometry of a droplet is a spherical cap on a substrate, which can be described in toroidal coordinates with toroid, spherical cap angle and azimuthal angle (α, β, ϕ). By taking $\alpha = \eta$, $\beta = \pi - \theta$ and $\phi = \Psi$, where η, θ and Ψ are defined in (Moon & Spencer 1971) for toroidal coordinates, the Cartesian coordinates (x, y, z) can be related to the toroidal coordinates by the following expressions

$$x = \frac{R \sinh\alpha \cos\phi}{\cosh\alpha + \cos\beta}, \quad y = \frac{R \sinh\alpha \sin\phi}{\cosh\alpha + \cos\beta}, \quad z = \frac{R \sin\beta}{\cosh\alpha + \cos\beta}, \qquad (2.1a{-}c)$$

https://doi.org/10.1017/jfm.2019.373 Published online by Cambridge University Press

where $\alpha \in [0, \infty)$, $\beta \in [0, \pi/2]$ and $\phi \in [0, 2\pi)$, and R is the radius of the spherical cap on the substrate surface. The metric coefficients are

$$h_\alpha = h_\beta = \frac{R}{\cosh\alpha + \cos\beta}, \quad h_\phi = \frac{R\sinh\alpha}{\cosh\alpha + \cos\beta}. \tag{2.2a,b}$$

Figure 1 is a view of two vertical planes of the toroidal coordinate system, showing the spherical cap of dimension $r^* \in [0, 1]$ and $z^* \in [0, 1]$ with the dimensionless radius r^* and height z^* defined as

$$r^* = \frac{\sqrt{x^2 + y^2}}{R}, \quad z^* = \frac{z}{R}. \tag{2.3a,b}$$

The UV light is incident on the surface of the droplet, which creates a surface tension gradient on the surface and drives the Marangoni flow inside the droplet. Shown in figure 2 are the different surface tension profiles corresponding linearly to UV laser profiles with peaks moving from the middle of the droplet to the edge, with or without O-masks. These beams are either Gaussian spot or ring. Based on these laser patterns, the surface tension profiles of azoTAB droplets are written as (Chevallier *et al.* 2011):

(1) Constant surface tension ring (CSTR) produced by an annular beam of constant intensity distribution

$$\sigma(r^*) - \sigma_0 = \Delta\sigma[H(r^* - p_1^*) - H(r^* - p_2^*)], \tag{2.4}$$

where H is the Heaviside function defined by

$$H(r*) = \begin{cases} 0 & r^* < 0 \\ 1 & r^* > 0. \end{cases} \tag{2.5}$$

(2) Gaussian surface tension spot (GSTS) or Gaussian surface tension ring (GSTR) produced by an annular beam of Gaussian intensity distribution (Zeng, Latham & Kar 2006)

$$\sigma(r^*) - \sigma_0 = \Delta\sigma\,\exp[-a(r^* - p^*)^2], \tag{2.6}$$

where σ_0 is the surface tension of droplets with trans-azoTAB, and $\Delta\sigma$ is the increase of surface tension under UV light. Here r^*, p_1^*, p_2^* and p^* are all dimensionless horizontal distances away from droplet centre. For case 1, from p_1^* to p_2^*, surface tension is higher than in other parts of the droplet. For cases 2 and 3, p^* represents the location of maximum surface tension. 'a' is related to the dimensionless beam width w^* by $w^* = 2\sqrt{2/a}$. In case 2, $a = 2$ represents Gaussian surface tension spot produced by overlapped Gaussian intensity distribution of an annular beam of small average radius. In case 3, $a = 1000$ represents a Gaussian surface tension ring produced by an annular beam of Gaussian intensity distribution (figure 2).

The characteristic velocity in the drop due to surface tension gradient can be expressed as

$$V_0 = \frac{\Delta\sigma}{\mu}, \tag{2.7}$$

https://doi.org/10.1017/jfm.2019.373 Published online by Cambridge University Press

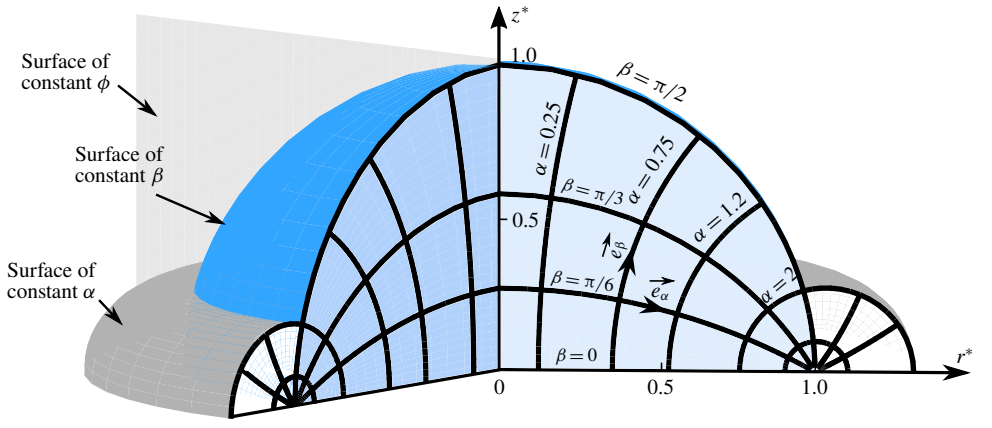


FIGURE 1. (Colour online) Illustration of toroidal coordinates for a spherical cap on a substrate.

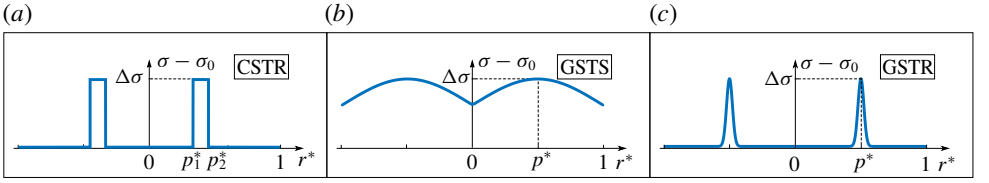


FIGURE 2. (Colour online) Sketch of surface tension profiles. (*a*) Case 1: Constant Surface Tension Ring (CSTR) with $p_1^* = 0.33$ and $p_2^* = 0.45$. (*b*) Case 2: Gaussian Surface Tension Spot (GSTS) with $p^* = 0.5$ and $a = 2$ for a beam width $w^* = 2$ to study the effect of broad illumination. (*c*) Case 3: Gaussian Surface Tension Ring (GSTR) with $p^* = 0.5$ and $a = 1000$ for a beam width $w^* = 0.089$ to study the effect of narrow illumination.

where μ is the dynamic viscosity of the solution. In ambient conditions, the characteristic velocity in the drop due to evaporation scales is (Gelderblom, Bloemen & Snoeijer 2012)

$$V_e(r^*) \sim A(\beta_c)\frac{\rho_g D(Y_s - Y_\infty)}{\rho R}(1 - r^*)^{\lambda(\beta_c)-1}, \tag{2.8}$$

where ρ is the density of the solution and ρ_g is the vapour density; D is the coefficient of binary diffusion of the vapour in the gas phase; Y_s and Y_∞ are the vapour mass fractions near the drop surface and far-field, respectively; and R is the radius of the drop. Here β_c denotes the droplet contact angle and $\lambda(\beta_c) = \pi/(2\pi - 2\beta_c)$ (Deegan *et al.* 1997). $A(\beta_c) \sim 1$ for large β_c in the current study. The characteristic velocity may be much larger at $r^* \to 1$ (i.e. $r^* > 0.99$).

For droplets of 10 mM azoTAB solution and ∼3 mm radius under controlled evaporation for 22.5 ± 1 °C and relative humidity of 45 ± 10 % (Lee, Smith & Hatton 2004; Varanakkottu *et al.* 2015), $V_0 \sim 1$ mm s^{-1} and $V_e \sim 10^{-4}$ mm s^{-1} from (2.7) and (2.8), respectively, and $V_e < V_0 \times 10^{-3}$ for $r^* < 0.99$. Since $V_e \ll V_0$ for the majority of the droplet, except near the contact line, evaporation is neglected in this study. For $Re \sim 2 \times 10^{-4}$, the problem is governed by the Stokes flow. The continuity

https://doi.org/10.1017/jfm.2019.373 Published online by Cambridge University Press

and vorticity equations for Stokes flow are

$$\boldsymbol{\nabla}\cdot\boldsymbol{V}=0, \tag{2.9}$$

$$\nabla^2\boldsymbol{\omega}=0. \tag{2.10}$$

The continuity equation in toroidal coordinates can be written as

$$\begin{aligned}\boldsymbol{\nabla}\cdot\boldsymbol{V} &= \frac{1}{h_\alpha h_\beta h_\phi}\left[\frac{\partial}{\partial\alpha}(h_\beta h_\phi V_\alpha)+\frac{\partial}{\partial\beta}(h_\alpha h_\phi V_\beta)\right]\\ &= \frac{(\cosh\alpha+\cos\beta)^2}{R\sinh\alpha}\left\{\frac{\partial}{\partial\alpha}\left[\frac{V_\alpha\sinh\alpha}{(\cosh\alpha+\cos\beta)^2}\right]+\frac{\partial}{\partial\beta}\left[\frac{V_\beta\sinh\alpha}{(\cosh\alpha+\cos\beta)^2}\right]\right\},\end{aligned} \tag{2.11}$$

where

$$V_\alpha=\frac{1}{h_\phi h_\beta}\frac{\partial\psi}{\partial\beta}=\frac{(\cosh\alpha+\cos\beta)^2}{R^2\sinh\alpha}\frac{\partial\psi}{\partial\beta}, \tag{2.12a}$$

$$V_\beta=-\frac{1}{h_\phi h_\alpha}\frac{\partial\psi}{\partial\alpha}=-\frac{(\cosh\alpha+\cos\beta)^2}{R^2\sinh\alpha}\frac{\partial\psi}{\partial\alpha}. \tag{2.12b}$$

For vorticity

$$\boldsymbol{\omega}=\boldsymbol{\nabla}\times\boldsymbol{V}=\hat{\boldsymbol{e}}_\phi\frac{1}{h_\phi}E^2\psi, \tag{2.13}$$

where

$$\begin{aligned}E^2 &= \frac{\sinh\alpha(\cosh\alpha+\cos\beta)}{R^2}\\ &\times\left[\frac{\partial}{\partial\alpha}\left(\frac{\cosh\alpha+\cos\beta}{\sinh\alpha}\frac{\partial}{\partial\alpha}\right)+\frac{\partial}{\partial\beta}\left(\frac{\cosh\alpha+\cos\beta}{\sinh\alpha}\frac{\partial}{\partial\beta}\right)\right].\end{aligned} \tag{2.14}$$

The vorticity equation in toroidal coordinates can be expressed in terms of ψ as

$$\nabla^2\boldsymbol{\omega}=\boldsymbol{\nabla}(\boldsymbol{\nabla}\cdot\boldsymbol{\omega})-\boldsymbol{\nabla}\times(\boldsymbol{\nabla}\times\boldsymbol{\omega})=-\boldsymbol{\nabla}\times(\boldsymbol{\nabla}\times\boldsymbol{\omega})=-\hat{\boldsymbol{e}}_\phi\frac{1}{h_\phi}E^2(E^2\psi). \tag{2.15}$$

Thus the governing equation for stream function corresponding to the vorticity equation in toroidal coordinates is

$$E^4\psi=0. \tag{2.16}$$

The general solution for (2.16) in toroidal coordinates has been given in several studies (El-Kareh & Secomb 1996; Masoud & Felske 2009*b*). To deal with non-homogeneous boundary conditions in the α-direction, Masoud & Felske (2009*b*) proposed a general solution with Gegenbauer functions serving as eigenfunctions in α-direction, which is given below:

$$\begin{aligned}\psi(\alpha,\beta) &= (\cosh\alpha+\cos\beta)^{-3/2}\int_0^\infty\left[A(\tau)C^{-1/2}_{1/2+\mathrm{i}\tau}(\cosh\alpha)+B(\tau)C^{*-1/2}_{1/2+\mathrm{i}\tau}(\cosh\alpha)\right]\\ &\times\left\{\sinh\tau\beta\left[C(\tau)\sin\beta+D(\tau)\cos\beta\right]\right.\\ &\left.+\cosh\tau\beta\left[E(\tau)\sin\beta+F(\tau)\cos\beta\right]\right\}\mathrm{d}\tau,\end{aligned} \tag{2.17}$$

where $C^{-1/2}_{1/2+\mathrm{i}\tau}(\cosh\alpha)$ and $C^{*-1/2}_{1/2+\mathrm{i}\tau}(\cosh\alpha)$ are the first and second kind Gegenbauer functions, respectively, of degree $-1/2$ and complex order $1/2+\mathrm{i}\tau$ with i as the imaginary unit (Happel & Brenner 2012).

https://doi.org/10.1017/jfm.2019.373 Published online by Cambridge University Press

2.2. *Boundary conditions and solution*

The boundary conditions for the stream function are obtained from the velocity boundary conditions. Normal to the rotation axis of symmetry, velocity is zero, i.e. $\boldsymbol{V}\cdot\hat{\boldsymbol{e}}_\alpha(0,\,\beta)=V_\alpha(0,\,\beta)=0$. On the substrate, the no slip boundary condition is $\boldsymbol{V}(\alpha,\,0)=\boldsymbol{0}$, i.e. $V_\alpha(\alpha,\,0)=0$ and $V_\beta(\alpha,\,0)=0$. Defining the value of β at the surface to be β_c, which is the contact angle, $\boldsymbol{V}\cdot\hat{\boldsymbol{e}}_\beta(\alpha,\,\beta_c)=V_\beta(\alpha,\,\beta_c)=0$ is assumed on the droplet surface. In the tangential direction of the droplet surface, surface tension and shear stress are balanced and, hence, $(\bar{\bar{\boldsymbol{\tau}}}\cdot\hat{\boldsymbol{n}})\cdot\hat{\boldsymbol{t}}=(\boldsymbol{\nabla}\sigma)\cdot\hat{\boldsymbol{t}}$, or $\tau_{\alpha\beta}=1/h_\alpha\partial\sigma/\partial\alpha|_{\beta_c}$. Where $\bar{\bar{\boldsymbol{\tau}}}$ is the stress tensor, $\hat{\boldsymbol{n}}$ and $\hat{\boldsymbol{t}}$ are the unit outward normal vector and unit tangential vector to the droplet surface, respectively. The tangential stress can be generated by laser illumination on the droplet surface utilizing the concentration-dependent and temperature-dependent surface tension to induce Marangoni convection in the droplet. The flow pattern can be modified by changing the surface tension gradient on the free surface of sessile drop and the gradient, in turn, can be altered by modulating the laser intensity distribution. This study explores a mechanism for generating streamlines on-demand for affecting the agglomeration of particles on the surface of a substrate.

Applying (2.12*a*) and (2.12*b*), boundary conditions of velocities normal to the boundaries are converted as follows:

$$V_\alpha(0,\,\beta)=0 \quad\Longrightarrow\quad \left.\frac{\partial\psi}{\partial\beta}\right|_{\alpha=0}=0 \quad\Longrightarrow\quad \psi(0,\,\beta)=C_1, \tag{2.18}$$

$$V_\beta(\alpha,\,0)=0 \quad\Longrightarrow\quad \left.\frac{\partial\psi}{\partial\alpha}\right|_{\beta=0}=0 \quad\Longrightarrow\quad \psi(\alpha,\,0)=C_2, \tag{2.19}$$

$$V_\beta(\alpha,\,\beta_c)=0 \quad\Longrightarrow\quad \left.\frac{\partial\psi}{\partial\alpha}\right|_{\beta=\beta_c}=0 \quad\Longrightarrow\quad \psi(\alpha,\,\beta_c)=C_3. \tag{2.20}$$

Since streamlines $\psi(0,\,\beta)$ connects with $\psi(\alpha,\,0)$ at point $(0,\,0)$ and $\psi(\alpha,\,\beta_c)$ at point $(0,\,\beta_c)$, we have that C_1, C_2 and C_3 are equal and set to 0. Thus,

$$\psi(0,\,\beta)=0, \tag{2.21}$$

$$\psi(\alpha,\,0)=0, \tag{2.22}$$

$$\psi(\alpha,\,\beta_c)=0. \tag{2.23}$$

The boundary condition $V_\alpha(\alpha,\,0)=0$ becomes

$$V_\alpha(\alpha,\,0)=0\Longrightarrow\left.\frac{\partial\psi}{\partial\beta}\right|_{\beta=0}=0. \tag{2.24}$$

Invoking the shear stress in toroidal coordinates (Moon & Spencer 1971),

$$\begin{aligned}\tau_{\alpha\beta}|_{\beta=\beta_c} &= \mu\left\{\frac{\partial}{\partial\alpha}\left[(\cosh\alpha+\cos\beta)\frac{V_\beta}{R}\right]+\frac{\partial}{\partial\beta}\left[(\cosh\alpha+\cos\beta)\frac{V_\alpha}{R}\right]\right\}\Bigg|_{\beta=\beta_c}\\ &= \mu\frac{(\cosh\alpha+\cos\beta_c)^2}{R^3\sinh\alpha}\left[(\cosh\alpha+\cos\beta_c)\frac{\partial^2\psi}{\partial\beta^2}-3\sin\beta_c\frac{\partial\psi}{\partial\beta}\right]\Bigg|_{\beta_c},\end{aligned} \tag{2.25}$$

the boundary condition $\tau_{\alpha\beta}=1/h_\alpha\partial\sigma/\partial\alpha|_{\beta_c}$ can be written as

$$\frac{(\cosh\alpha+\cos\beta_c)}{R^2\sinh\alpha}\left[(\cosh\alpha+\cos\beta_c)\,\frac{\partial^2\psi}{\partial\beta^2}-3\sin\beta_c\frac{\partial\psi}{\partial\beta}\right]\Bigg|_{\beta_c}=\frac{1}{\mu}\left.\frac{\partial\sigma}{\partial\alpha}\right|_{\beta_c}. \tag{2.26}$$

https://doi.org/10.1017/jfm.2019.373 Published online by Cambridge University Press

The other three boundary conditions are non-singular boundary conditions at the axis of symmetry as well as at the contact line. The velocities are finite

$$V_\beta(0,\beta)=\text{finite},\quad V_\alpha(\alpha\to\infty,\beta)=\text{finite},\quad V_\beta(\alpha\to\infty,\beta)=\text{finite},\qquad (2.27a{-}c)$$

therefore

$$\left.\frac{(\cosh\alpha+\cos\beta)^2}{R^2\sinh\alpha}\frac{\partial\psi}{\partial\alpha}\right|_{\alpha=0}=\text{finite},\qquad (2.28a)$$

$$\left.\frac{(\cosh\alpha+\cos\beta)^2}{R^2\sinh\alpha}\frac{\partial\psi}{\partial\beta}\right|_{\alpha\to\infty}=\text{finite},\qquad (2.28b)$$

$$\left.\frac{(\cosh\alpha+\cos\beta)^2}{R^2\sinh\alpha}\frac{\partial\psi}{\partial\alpha}\right|_{\alpha\to\infty}=\text{finite}.\qquad (2.28c)$$

Applying boundary conditions (2.21) in (2.17), $B(\tau)=0$ for $C^{*\,-1/2}_{1/2+\mathrm{i}\tau}(\cosh\alpha)|_{\alpha=0}\neq 0$ (Masoud & Felske 2009*a*). It also follows from (2.22) that $F(\tau)=0$. Then from (2.24),

$$E(\tau)=-\tau D(\tau).\qquad (2.29)$$

Inserting the above results into (2.17), the stream function becomes

$$\psi(\alpha,\beta)=(\cosh\alpha+\cos\beta)^{-3/2}\int_0^\infty K(\beta,\tau)C^{-1/2}_{1/2+\mathrm{i}\tau}(\cosh\alpha)\,\mathrm{d}\tau,\qquad (2.30)$$

where

$$K(\beta,\tau)=k_1(\tau)\sin\beta\sinh(\tau\beta)+k_2(\tau)\big[\cos\beta\sinh(\tau\beta)-\tau\sin\beta\cosh(\tau\beta)\big].\qquad (2.31)$$

Non-singular boundary conditions, equations (2.28), can be checked by asymptotic analysis. Note that (Happel & Brenner 2012)

$$\begin{aligned}\frac{(\cosh\alpha+\cos\beta)^2}{R^2\sinh\alpha}\frac{\partial\psi}{\partial\alpha}&=-\frac{3(\cosh\alpha+\cos\beta)^{-1/2}}{2R^2}\int_0^\infty K(\beta,\tau)C^{-1/2}_{1/2+\mathrm{i}\tau}(\cosh\alpha)\,\mathrm{d}\tau\\&\quad-\frac{(\cosh\alpha+\cos\beta)^{1/2}}{R^2}\int_0^\infty K(\beta,\tau)P_{-1/2+\mathrm{i}\tau}(\cosh\alpha)\,\mathrm{d}\tau\end{aligned}\qquad (2.32)$$

and

$$\begin{aligned}\frac{(\cosh\alpha+\cos\beta)^2}{R^2\sinh\alpha}\frac{\partial\psi}{\partial\beta}&=-\frac{3(\cosh\alpha+\cos\beta)^{-1/2}\sin\beta}{2R^2\sinh\alpha}\int_0^\infty K(\beta,\tau)C^{-1/2}_{1/2+\mathrm{i}\tau}(\cosh\alpha)\,\mathrm{d}\tau\\&\quad+\frac{(\cosh\alpha+\cos\beta)^{1/2}}{R^2\sinh\alpha}\int_0^\infty\frac{\partial K}{\partial\beta}C^{-1/2}_{1/2+\mathrm{i}\tau}(\cosh\alpha)\,\mathrm{d}\tau.\end{aligned}\qquad (2.33)$$

With $C^{-1/2}_{1/2+\mathrm{i}\tau}(\cosh\alpha)\sim O(\cosh^{1/2}\alpha)$ and $P_{-1/2+\mathrm{i}\tau}(\cosh\alpha)\sim O(\cosh^{-1/2}\alpha)$ when $\alpha\to\infty$ (Silverman *et al.* 1972), equations (2.28*a–c*) are satisfied automatically.

https://doi.org/10.1017/jfm.2019.373 Published online by Cambridge University Press

By applying (2.23), the relationship of $k_1(\tau)$ and $k_2(\tau)$ can be shown as

$$k_2(\tau) = -k_1(\tau)\frac{\sin\beta_c \sinh(\tau\beta_c)}{\cos\beta_c \sinh(\tau\beta_c) - \tau \sin\beta_c \cosh(\tau\beta_c)}. \tag{2.34}$$

Next, by substituting the integral transfer relationship (Masoud & Felske 2009*a*) in (2.30)

$$K(\beta, \tau) = \tau\left(\tau^2 + \frac{1}{4}\right)\tanh(\pi\tau)\int_0^\infty \frac{\psi(\alpha, \beta)(\cosh\alpha + \cos\beta)^{3/2}}{\sinh\alpha} C^{-1/2}_{1/2+i\tau}(\cosh\alpha)\,\mathrm{d}\alpha. \tag{2.35}$$

Applying the operator $\partial^2/\partial\beta^2$ on both sides of (2.35) at $\beta = \beta_c$

$$\left.\frac{\partial^2 K}{\partial\beta^2}\right|_{\beta_c} = \tau\left(\tau^2 + \frac{1}{4}\right)\tanh(\pi\tau) \times \int_0^\infty \left.\frac{\partial^2}{\partial\beta^2}[\psi(\alpha, \beta)(\cosh\alpha + \cos\beta)^{3/2}]\right|_{\beta_c} \frac{C^{-1/2}_{1/2+i\tau}(\cosh\alpha)}{\sinh\alpha}\,\mathrm{d}\alpha. \tag{2.36}$$

By invoking (2.23) and the last boundary condition, (2.26), $\partial^2/\partial\beta^2\left[\psi(\alpha, \beta)(\cosh\alpha + \cos\beta)^{3/2}\right]\big|_{\beta_c}$ can be simplified as

$$\begin{aligned}
&\left.\frac{\partial^2}{\partial\beta^2}[\psi(\alpha, \beta)(\cosh\alpha + \cos\beta)^{3/2}]\right|_{\beta_c} \\
&= (\cosh\alpha + \cos\beta)^{1/2}\left[(\cosh\alpha + \cos\beta)\frac{\partial^2\psi}{\partial\beta^2} - 3\sin\beta\,\frac{\partial\psi}{\partial\beta}\right]\Bigg|_{\beta_c} \\
&= R^2 \sinh\alpha(\cosh\alpha + \cos\beta_c)^{-1/2}\left.\frac{\partial\sigma}{\mu\partial\alpha}\right|_{\beta_c}.
\end{aligned} \tag{2.37}$$

By inserting (2.37) and (2.34) into (2.36) for $\beta = \beta_c$, we can solve for $k_1(\tau)$ with

$$k_1(\tau) = \frac{N_1 N_2}{M_1 + M_2 M_3}, \tag{2.38}$$

where

$$N_1 = \tau\left(\tau^2 + \tfrac{1}{4}\right)\tanh(\pi\tau), \tag{2.39a}$$

$$N_2 = \int_0^\infty R^2(\cosh\alpha' + \cos\beta_c)^{-1/2}\left.\frac{\partial\sigma}{\mu\partial\alpha'}\right|_{\beta_c} C^{-1/2}_{1/2+i\tau}(\cosh\alpha')\,\mathrm{d}\alpha', \tag{2.39b}$$

$$M_1 = 2\tau\cos\beta_c\cosh(\tau\beta_c) + (\tau^2 - 1)\sin\beta_c\sinh(\tau\beta_c), \tag{2.39c}$$

$$M_2 = (\tau^2 + 1)\cos\beta_c\sinh(\tau\beta_c) + (\tau + \tau^3)\sin\beta_c\cosh(\tau\beta_c), \tag{2.39d}$$

$$M_3 = \frac{\sin\beta_c\sinh(\tau\beta_c)}{\cos\beta_c\sinh(\tau\beta_c) - \tau\sin\beta_c\cosh(\tau\beta_c)}. \tag{2.39e}$$

Nondimentionalizing $\psi(\alpha, \beta)$ by $\psi_0 = R^2\Delta\sigma/\mu$

$$\psi^*(\alpha, \beta) = \frac{\psi}{\psi_0} = (\cosh\alpha + \cos\beta)^{-3/2}\int_0^\infty K^*(\beta, \tau)C^{-1/2}_{1/2+i\tau}(\cosh\alpha)\,\mathrm{d}\tau, \tag{2.40}$$

https://doi.org/10.1017/jfm.2019.373 Published online by Cambridge University Press

with

$$K^*(\beta,\tau) = \Big[\sin\beta\sinh(\tau\beta) - \sin\beta_c\sinh(\tau\beta_c) \times \frac{\cos\beta\sinh(\tau\beta) - \tau\sin\beta\cosh(\tau\beta)}{\cos\beta_c\sinh(\tau\beta_c) - \tau\sin\beta_c\cosh(\tau\beta_c)}\Big] k_1^*(\tau), \tag{2.41}$$

where the expression for $k_1^*(\tau)$ is the same as $k_1(\tau)$ with N_2 replaced by N_2^*, and

$$N_2^* = \int_0^\infty (\cosh\alpha' + \cos\beta_c)^{-1/2} \frac{1}{\Delta\sigma}\frac{\partial\sigma}{\partial\alpha'}\bigg|_{\beta_c} C_{1/2+i\tau}^{-1/2}(\cosh\alpha')\,\mathrm{d}\alpha'. \tag{2.42}$$

One of the advantages of developing an analytical solution is that one can predict the effect of different surface tension distributions in toroidal coordinates. The effect of light illumination on the stream function appears in (2.42) through the surface tension profiles given in (2.4) and (2.6). The solution can be used to find the number of vortices and dividing streamlines that allow unique deposition patterns for the specified surface tension profile. It is also possible to find the solution in isolated areas, such as near the contact line or the substrate.

For the Heaviside step function in (2.4), surface tension gradient $\partial\sigma/\partial\alpha$ becomes the Dirac delta function and therefore N_2^* can be written as

$$N_2^* = (\cosh\alpha_1 + \cos\beta_c)^{-1/2} C_{1/2+i\tau}^{-1/2}(\cosh\alpha_1) - (\cosh\alpha_2 + \cos\beta_c)^{-1/2} C_{1/2+i\tau}^{-1/2}(\cosh\alpha_2), \tag{2.43}$$

where α_1 and α_2 are the toroids of the points at $r^* = p_1^*$ and $r^* = p_2^*$, respectively, on the droplet surface where $\beta = \beta_c$. Using (2.1) and (2.3), α_1 and α_2 are obtained as

$$\cosh\alpha_1 = \frac{\cos\beta_c + \sqrt{\cos^2\beta_c + (p_1^{*-2} - 1)(\cos^2\beta_c + p_1^{*-2})}}{p_1^{*-2} - 1}, \tag{2.44a}$$

$$\cosh\alpha_2 = \frac{\cos\beta_c + \sqrt{\cos^2\beta_c + (p_2^{*-2} - 1)(\cos^2\beta_c + p_2^{*-2})}}{p_2^{*-2} - 1}. \tag{2.44b}$$

In (2.40), α varies up to ∞ since the physical dimension of the droplet, r^*, which varies from 0 to 1, is transformed by the toroid α to an infinite range of $\alpha \in [1, \infty)$ in toroidal coordinates. However, $\alpha = 6$ corresponds to $r^* = 0.995$ which approximates the position of the contact line with a high degree of accuracy, therefore α is taken to be six for calculating the stream function near the contact line. In (2.42), the integration represents the effect of the boundary condition, i.e. the surface tension gradient for all possible values of the toroid α' extending up to ∞ as the upper limit of integration, but the maximum value of α' can be taken as six since it corresponds to $r^* = 0.995$.

For the Gaussian surface tension profile in (2.6), (2.42) is evaluated numerically by approximating the infinite upper limit of the integration to a finite value $\alpha'_{max} = 6$. Here (2.42) is integrated numerically using the Trapezoidal rule for each value of τ and β_c by taking the interval of numerical integration $\Delta\alpha' = 0.01$ and 0.001 for the cases in figures 2(*b*) and 2(*c*), respectively, and the resulting N_2^* is substituted in (2.40). Generally, the results of the integration oscillate due to Gibbs' phenomenon when the infinite upper limit of integration is replaced with finite values and the

https://doi.org/10.1017/jfm.2019.373 Published online by Cambridge University Press

integration represents the solution of a physical problem involving a discontinuity such as a discontinuous boundary condition. In the present case, the integrand decays rapidly due to the exponential term in the Gaussian profile. Therefore, the result of (2.42) is expected to be free of Gibbs' oscillation.

Using (2.40), the dimensionless stream function ψ^* is calculated by approximating the infinite upper limit to a finite value τ_{max}. Due to this approximation, the stream function would also exhibit Gibbs' oscillation as in the case of (2.42). For example, spurious vortices were observed in the droplet when $\tau_{max} = 50$ for case 3 in figure 2(*c*) (Gaussian Surface Tension Ring) and these spurious vortices disappear for sufficiently large values of τ_{max}. Therefore ψ^* has been determined by taking τ_{max} as 900, 50 and 200 for cases 1, 2 and 3, respectively, and the numerical integration interval $\Delta\tau$ as 0.1 for all cases. Identical flow patterns were observed for higher values of τ_{max} and lower values of $\Delta\tau$.

Here τ_{max} is very high for case 1 because of the sharp discontinuity in the surface tension profile represented by the Heaviside function (2.4). On the other hand, τ_{max} is fairly low for case 2 since a broad Gaussian function (2.6) with a value of $a = 2$ represents the surface tension profile as a slowly varying slope. In case 3, however, τ_{max} is higher than in case 2 since a narrow Gaussian function (2.6) represents the surface tension profile with a steeper slope than in case 2. The value of $\Delta\tau$ depends upon the periodicity of the Gegenbauer function $C^{-1/2}_{1/2+i\tau}(\cosh\alpha)$ with respect to τ for a fixed value of α, and this function oscillates rapidly with short periodicity for large values of α (El-Kareh & Secomb 1996). In the present study, the shortest periodicity was found to be 1.1 for $\alpha = 6$, and the value of $\Delta\tau = 0.1$ corresponds to taking 11 points within one period of the oscillation. In (2.40), the above-mentioned values of τ_{max} and $\Delta\tau$ yield convergent solutions in most of the droplet volume except near the free surface where the integrand decays very slowly and Gibbs' oscillation may exist.

3. Results

In this section, flow patterns inside the droplet of azoTAB solution are evaluated for different UV light patterns as well as for different contact angles. First, two experimental cases are used to validate the current analytical results and then the formation of vortices are analysed by varying the profiles of light illumination on the droplet.

3.1. *Experimental Validation*

Experiment 1: In this experiment, a spherical cap droplet of radius 3 mm and contact angle 0.21π with 10 mM azoTAB concentration undergoes Marangoni convection due to UV light illumination through a transparent ring in a mask. The inner and outer radii of the transparent ring are 1.0 and 1.35 mm, respectively (Varanakkottu *et al.* 2015). At the end of the experiment, the carboxylate polystyrene particles are deposited on the substrate as a ring of radius 1.13 mm with a width of 0.27 mm. A supporting video is given in their paper where the deposition occurs in half the time (25 min) compared to evaporation (50 min).

This experimental condition is simulated by considering a spherical cap droplet of contact angle 0.21π and a Constant Surface Tension Ring (case 1 in figure 2*a*) of dimensionless inner and outer radii $p_1^* = 0.33$ and $p_2^* = 0.45$, respectively, corresponding to the radii of the UV illumination through the transparent ring of the mask. The analytical solution for the stream function under this condition is presented in figure 3, showing two counter-rotating eddies of almost equal strength

https://doi.org/10.1017/jfm.2019.373 Published online by Cambridge University Press

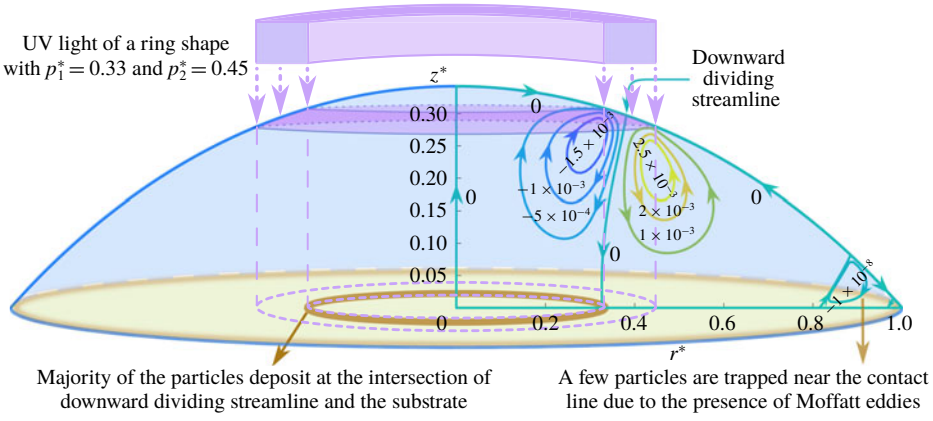


FIGURE 3. (Colour online) Stream function and deposition prediction for Constant Surface Tension Ring with $p_1^* = 0.33$, $p_2^* = 0.45$ and $\beta_c = 0.21\pi$. Particles are gathered by the contour-rotating circulations and deposited on the substrate by the downward dividing streamline, forming a ring. A few particles are trapped near the contact line due to the Moffatt eddies.

around $r^* = 0.35$. The majority of the particles are expected to be gathered by the counter-rotating eddies and follow the downward dividing streamline between the eddies, $\psi^* = 0$, to deposit on the substrate. The locus of the contact point between the downward dividing streamline and the substrate forms a ring around the axis of symmetry.

In figure 4, the contact angles in the droplet are changed from 0.21π to $\pi/9$ to simulate the changes in the droplet height due to evaporation during the deposition. This reduction in height is accounted for by varying the contact angle. By calculating the stream functions of series of contact angle from 0.21π to $\pi/9$, the changes in the position of intersection between the downward streamline and substrate, defined as deposition position D^*, can be tracked. D^* shifts toward the contact line from $D^* = 0.33$ to 0.37 for the contact angles decreasing from 0.21π to $\pi/9$ (figures 4*a* and 4*b*). Therefore, the deposited particles are expected to form a deposition ring of finite width during the period of deposition when the contact angle changes in the above-mentioned range. The current analysis predicts the location of the particle deposition given by the dimensionless radius of the centre line of the deposition ring, 0.35, i.e. 1.05 mm, which matches very well with the experimental result. The dimensionless width of the deposition ring is found to be 0.04, i.e. 0.12 mm, which also appears to be well-predicted within experimental uncertainty and the striations on the ring as shown in figure 4(*c*). The other eddies appearing in figures 3 and 4 are discussed at the end of this section.

Experiment 2: A spherical cap droplet of radius 2.3 mm and contact angle 0.21π with 10 mM azoTAB concentration undergoes Marangoni convection due to UV light located above the droplet centre with a beam width of 165 μm (Varanakkottu *et al.* 2015). At the end of the experiment cationic particles deposit on the substrate as a dot at the droplet centre.

In the corresponding analytical solution, shown in figure 4(*d*), a constant surface tension spot of dimensionless width $w^* = 0.072$ located at the droplet centre is used

https://doi.org/10.1017/jfm.2019.373 Published online by Cambridge University Press

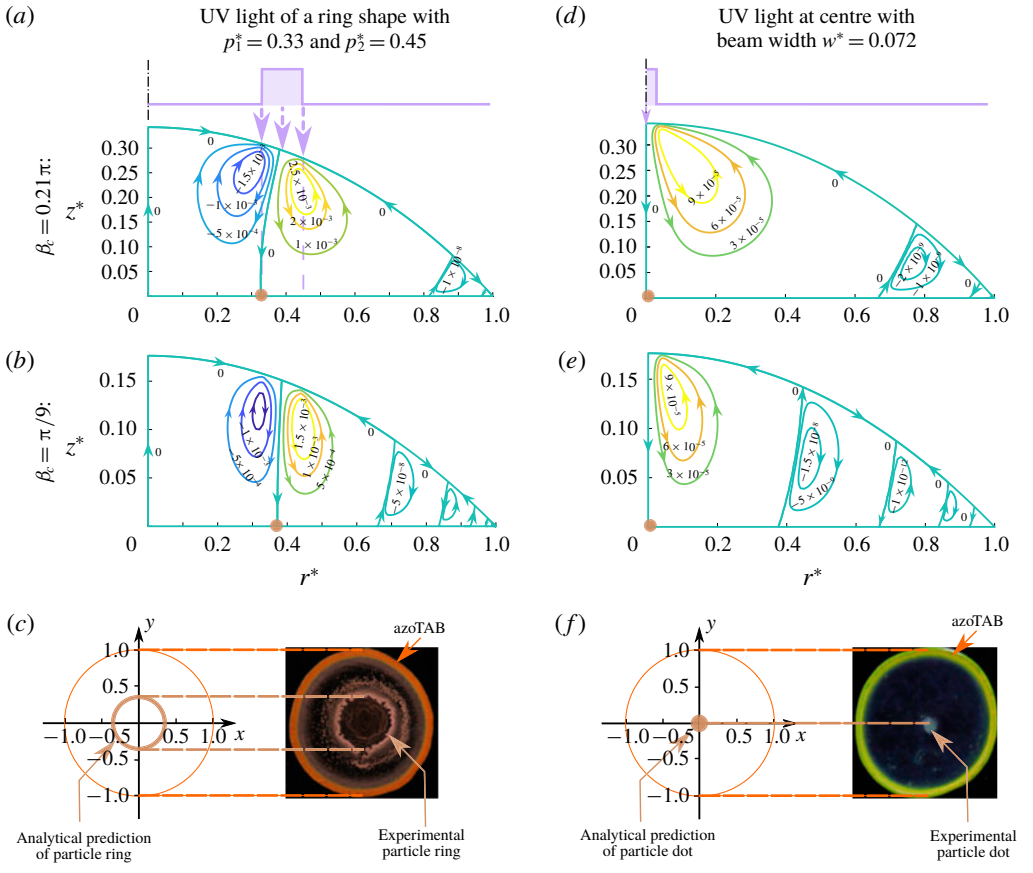


FIGURE 4. (Colour online) Comparison of the particle deposition patterns in the experiments (Varanakkottu *et al.* 2015) and analytical solutions for droplets under UV light. Reprinted with permission from (Varanakkottu *et al.* 2015). Copyright (2016) American Chemical Society. (*a*,*b*) Stream functions and depositions of carboxylate polystyrene particles on the substrate by UV light of a ring shape for contact angle $\beta_c = 0.21\pi$ and $\beta_c = \pi/9$ respectively. (*c*) Comparison of particle deposition between the analytical solution and in experiments by UV light of a ring shape. (*d*,*e*) Stream functions and cationic particle depositions on the substrate with UV beam at drop centre for contact angle $\beta_c = 0.21\pi$ and $\beta_c = \pi/9$, respectively. (*f*) Comparison of particle deposition between the analytical solution and in experiments by UV light at drop centre.

to simulate the laser spot size and location in the experiment. This analysis is also performed for decreasing contact angles from 0.21π to $\pi/9$ (figures 4*d* and 4*f*) as done in figures 4(*a*) and 4(*b*). The deposition region D^* remains zero for contact angle decreasing from 0.21π to $\pi/9$ indicating that particles are expected to deposit on the substrate as a dot at the droplet centre. Thus, the predicted deposition locations from the analytical solutions agree with both available experimental results.

Shown in both figures 3 and 4, the primary circulations appear near where the surface tension is high and undergoes a toroidal rotation while a series of weak vortices, which are Moffatt eddies, forms near the contact line.

https://doi.org/10.1017/jfm.2019.373 Published online by Cambridge University Press

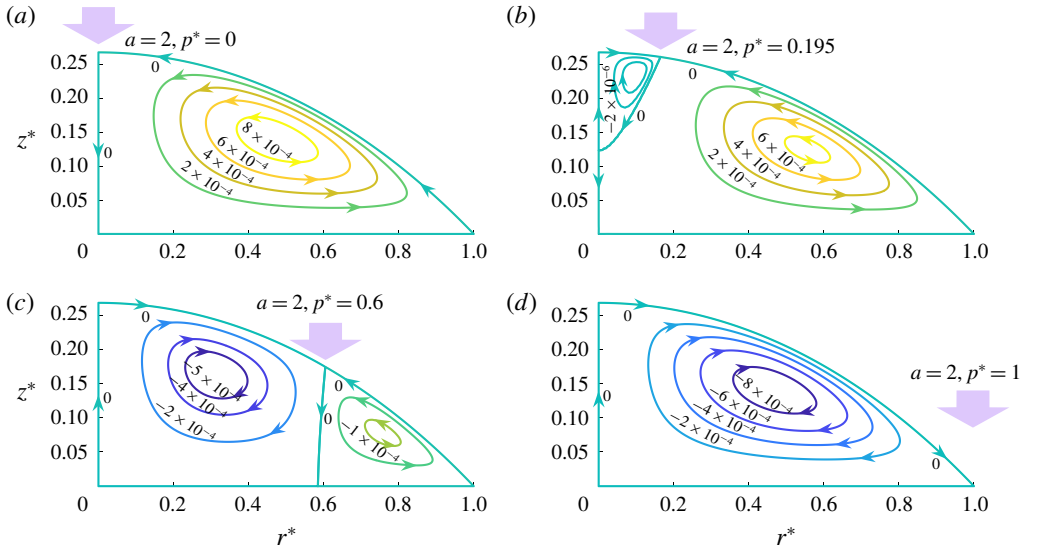


FIGURE 5. (Colour online) Contour of dimensionless stream function for case 2 with $a = 2$. The geometry of the droplet is $R = 1$ mm, contact angle $\beta_c = \pi/6$. The arrow indicates the peak intensity position of the laser incident on the droplet. The azoTAB concentration is 10 mM. (*a*) Position of the peak is $p^* = 0$. A large toroidal circulation (counter-clockwise on paper) is formed. (*b*) At $p^* = 0.195$, a new counter-rotating toroidal circulation is formed at the top centre. (*c*) At $p^* = 0.6$, this counter-rotating circulation near the centre grows, and the original circulation (counter-clockwise on paper) diminishes in size. (*d*) At the droplet edge, the stronger counter-rotating circulation completely takes over the droplet.

3.2. *Marangoni convection patterns for different surface tension profiles:*

After validating the analytical solution for case 1, the effects of light modulation by varying p^* and a for cases 2 and 3 are evaluated. The resulting flow patterns due to different surface tension profiles are expected to agglomerate the particles to certain selected regions on the substrate.

(1) Effect of broad Gaussian illumination: This effect is examined for Gaussian Surface Tension Spot using (2.6) (case 2 in figure 2*b*), varying p^* and constant a. $R = 1$ mm; contact angle $\beta_c = \pi/6$; azoTAB concentration $= 10$ mM; $a = 2$; $\sigma_0 = 43$ mN m^{-1}; $\Delta\sigma = 5$ mN m^{-1}. By varying p^* from 0 to 1, the flow pattern in the droplet changes from a toroidal circulation (appears as counter-clockwise circulation in figure 5*a*) to a clockwise toroidal cell near the top of the droplet (figure 5*b*), growing to a larger volume (figure 5*c*) and eventually to a single clockwise cell (figure 5*d*). This type of modulation in the circulation pattern, which has not been observed or reported previously, provides the requisite Marangoni circulation to obtain various deposition patterns on demand.

For the same case as in figure 5, a flow regime map is developed to understand various circulation patterns for different values of the Gaussian beam position p^* and the droplet contact angle β_c. When the peak of the beam is shifted from the centre of the droplet to its edge, i.e. p^* is varied from 0 to 1, the orientation of circulation changes as a function of β_c. A large single counter-clockwise circulation appears when p^* is less than certain values depending on β_c and the boundary of this phenomenon

https://doi.org/10.1017/jfm.2019.373 Published online by Cambridge University Press

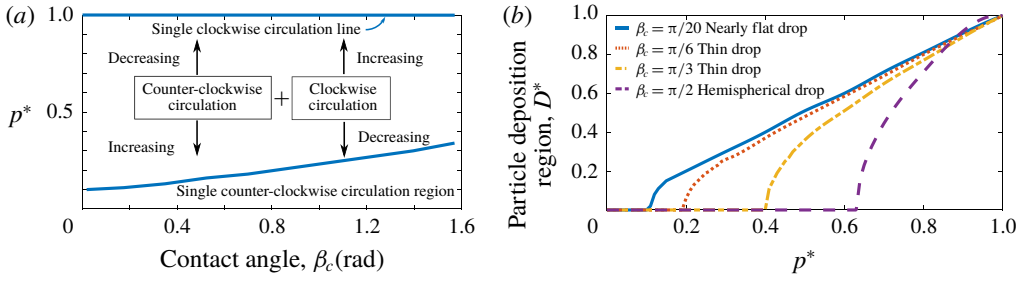


FIGURE 6. (Colour online) (*a*) Single counter-clockwise circulation region, twin circulation region and single clockwise circulation line determined by surface tension peak p^* and contact angle β_c for case 2 with $a = 2$. (*b*) Relationship of deposition region D^* and surface tension peak p^* for case 2 with $a = 2$.

is shown in figure 6(*a*). Above this boundary, i.e. when the peak of the beam is in the mid-section of the droplet, both counter-clockwise and clockwise circulations appear in the droplet. As p^* increases, however, the size and strength of the counter-clockwise circulation decreases while the clockwise circulation becomes larger and stronger. When the peak of the beam is shifted at the edge of the droplet, i.e. $p^* = 1$, a large single clockwise circulation dominates the Marangoni convection.

Figure 6(*b*) shows the particle deposition position D^* as a function of p^*. For $\beta_c = \pi/6$ as an example, deposition occurs at the droplet centre as D^* remains zero for $p^* \leqslant 0.19$; then for a small shift in the beam peak, i.e. from $p^* = 0.19$ to 0.23, D^* rapidly shifts to 0.15 and from this point on until the beam reaches the droplet edge the profile stays linear. This is seen for all cases, however for smaller β_c, a smaller beam shift is needed to start a clockwise toroidal circulation and to achieve the rapidly and linearly increasing region of D^*.

(2) Effect of narrow Gaussian illumination: For Gaussian Surface Tension Ring using (2.4) (case 3 in figure 2*c*), the effect of narrow illumination is evaluated by changing the beam position p^* and constant a. $R = 1$ mm; contact angle $\beta_c = \pi/6$; azoTAB concentration = 10 mM; $a = 1000$; $\sigma_0 = 43$ mN m^{-1}; $\Delta\sigma = 5$ mN m^{-1}. Figure 7 shows two cases of stream function under (2.4), with $a = 1000$, beam peak at $p^* = 0$ (figure 7*a*) and $p^* = 0.5$ (figure 7*b*). The effect of narrow Gaussian Surface Tension Ring on the flow patterns is similar to that of Constant Surface Tension Ring (figure 3 and figure 4) in generating the primary circulations near the beam peak with Moffatt eddies occurring away from the beam peak.

4. Conclusion

An analytical solution is developed to determine the stream function in sessile azoTAB droplets for different surface tension gradients produced by different intensity distributions of UV light. The downward dividing streamline is expected to deposit the particles on the substrate. The solution to a biharmonic stream function equation has yielded multiple cells. The downward dividing streamlines are expected to deposit particles as dots at the droplet centre or as rings around the axisymmetric axis. These dots and rings predict the experimental results very well. The effect of broad UV illumination on the position of the downward dividing streamline (i.e. possible position of particle agglomeration) is studied using Gaussian Surface Tension Spot by varying the position of the peak intensity p^* and the contact angle

https://doi.org/10.1017/jfm.2019.373 Published online by Cambridge University Press

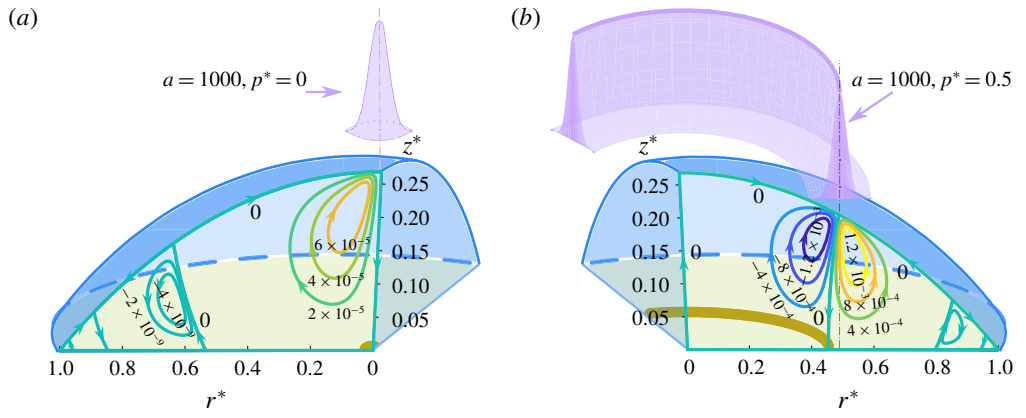


FIGURE 7. (Colour online) Contour of dimensionless stream function by narrow illuminations for case 3 with contact angle $\beta_c = \pi/6$, $a = 1000$: (*a*) Surface tension peak is set as $p^* = 0$. (*b*) Surface tension peak is set as $p^* = 0.5$.

β_c of droplets. The resultant flow regime map reveals that the circulations change from counter-clockwise at $p^* < 0.15$ to clockwise at $p^* = 1$ for the contact angle of $\beta_c = \pi/6$. The values of p^* affect the size and number of circulations. The effect of contact angle is also studied and a single counter-clockwise circulation is found to occur below certain critical values of p^*, both counter-clockwise and clockwise circulations occur above these critical values leading to a single clockwise circulation at $p^* = 1$. Narrow Gaussian UV light illumination at the droplet centre produces localized primary circulation centred at the droplet centre along with weaker secondary circulations called Moffatt eddies. A similar effect is also observed when the illumination is centred half way from the droplet centre producing a narrow Gaussian surface tension ring.

Acknowledgements

This work was partially supported by the National Science Foundation, CMMI, MME (1563448).

REFERENCES

ANYFANTAKIS, M. & BAIGL, D. 2014 Dynamic photocontrol of the coffee-ring effect with optically tunable particle stickiness. *Angewandte Chemie* **126** (51), 14301–14305.

ANYFANTAKIS, M., VARANAKKOTTU, S. N., RUDIUK, S., MOREL, M. & BAIGL, D. 2017 Evaporative optical Marangoni assembly: tailoring the three-dimensional morphology of individual deposits of nanoparticles from sessile drops. *ACS Appl. Mater. Interfaces* **9** (42), 37435–37445.

ARMSTRONG, E., KHUNSIN, W., OSIAK, M., BLÖMKER, M., TORRES, C. M. S. & O'DWYER, C. 2014 Ordered 2D colloidal photonic crystals on gold substrates by surfactant-assisted fast-rate dip coating. *Small* **10** (10), 1895–1901.

BISWAS, S. & KALITA, J. C. 2018 Moffatt eddies in the driven cavity: a quantification study by an HOC approach. *Comput. Maths Applics.* **76** (3), 471–487.

BROWN, P., BUTTS, C. P. & EASTOE, J. 2013 Stimuli-responsive surfactants. *Soft Matt.* **9** (8), 2365–2374.

https://doi.org/10.1017/jfm.2019.373 Published online by Cambridge University Press

CHEVALLIER, E., MAMANE, A., STONE, H. A., TRIBET, C., LEQUEUX, F. & MONTEUX, C. 2011 Pumping-out photo-surfactants from an air–water interface using light. *Soft Matt.* **7** (17), 7866–7874.

DEEGAN, R. D. 2000 Pattern formation in drying drops. *Phys. Rev. E* **61** (1), 475–485.

DEEGAN, R. D., BAKAJIN, O., DUPONT, T. F., HUBER, G., NAGEL, S. R. & WITTEN, T. A. 1997 Capillary flow as the cause of ring stains from dried liquid drops. *Nature* **389** (6653), 827–829.

DIDDENS, C., TAN, H., LV, P., VERSLUIS, M., KUERTEN, J. G. M., ZHANG, X. & LOHSE, D. 2017 Evaporating pure, binary and ternary droplets: thermal effects and axial symmetry breaking. *J. Fluid Mech.* **823**, 470–497.

EL-KAREH, A. W. & SECOMB, T. W. 1996 Stokes flow impinging on a spherical cap on a plane wall. *Q. J. Mech. Appl. Maths* **49** (2), 179–183.

FISCHER, B. J. 2002 Particle convection in an evaporating colloidal droplet. *Langmuir* **18** (1), 60–67.

GELDERBLOM, H., BLOEMEN, O. & SNOEIJER, J. H. 2012 Stokes flow near the contact line of an evaporating drop. *J. Fluid Mech.* **709**, 69–84.

HAPPEL, J. & BRENNER, H. 2012 *Low Reynolds Number Hydrodynamics: with Special Applications to Particulate Media*, vol. 1. Springer Science & Business Media.

HU, H. & LARSON, R. G. 2005*a* Analysis of the effects of Marangoni stresses on the microflow in an evaporating sessile droplet. *Langmuir* **21** (9), 3972–3980.

HU, H. & LARSON, R. G. 2005*b* Analysis of the microfluid flow in an evaporating sessile droplet. *Langmuir* **21** (9), 3963–3971.

HUANG, X., ZHOU, J., FU, M., LI, B., WANG, Y., ZHAO, Q., YANG, Z., XIE, Q. & LI, L. 2007 Binary colloidal crystals with a wide range of size ratios via template-assisted electric-field-induced assembly. *Langmuir* **23** (17), 8695–8698.

JEONG, J.-T. & MOFFATT, H. K. 1992 Free-surface cusps associated with flow at low Reynolds number. *J. Fluid Mech.* **241**, 1–22.

KIM, J. J., LI, Y., LEE, E. J. & CHO, S. O. 2011 Fabrication of size-controllable hexagonal non-close-packed colloidal crystals and binary colloidal crystals by pyrolysis combined with plasma-electron coirradiation of polystyrene colloidal monolayer. *Langmuir* **27** (6), 2334–2339.

LEE, C. T., SMITH, K. A. & HATTON, T. A. 2004 Photoreversible viscosity changes and gelation in mixtures of hydrophobically modified polyelectrolytes and photosensitive surfactants. *Macromolecules* **37** (14), 5397–5405.

MARIN, A., LIEPELT, R., ROSSI, M. & KÄHLER, C. J. 2016 Surfactant-driven flow transitions in evaporating droplets. *Soft Matt.* **12** (5), 1593–1600.

MASOUD, H. & FELSKE, J. D. 2009*a* Analytical solution for inviscid flow inside an evaporating sessile drop. *Phys. Rev. E* **79** (1), 016301.

MASOUD, H. & FELSKE, J. D. 2009*b* Analytical solution for stokes flow inside an evaporating sessile drop: Spherical and cylindrical cap shapes. *Phys. Fluids* **21** (4), 042102.

MOFFATT, H. K. 1964 Viscous and resistive eddies near a sharp corner. *J. Fluid Mech.* **18**, 1.

MOON, P. & SPENCER, D. E. 1971 *Field Theory Handbook: Including Coordinate Systems, Differential Equations and their Solutions*. Springer.

RISTENPART, W. D., KIM, P. G., DOMINGUES, C., WAN, J. & STONE, H. A. 2007 Influence of substrate conductivity on circulation reversal in evaporating drops. *Phys. Rev. Lett.* **99** (23), 234502.

SCRIVEN, L. E. & STERNLING, C. V. 1964 On cellular convection driven by surface-tension gradients: effects of mean surface tension and surface viscosity. *J. Fluid Mech.* **19** (3), 321–340.

SHANKAR, P. N. 1993 The eddy structure in stokes flow in a cavity. *J. Fluid Mech.* **250**, 371–383.

SHTERN, V. 2018 *Cellular Flows: Topological Metamorphoses in Fluid Mechanics*. Cambridge University Press.

SILVERMAN, R. A. & OTHERS 1972 *Special Functions and their Applications*. Courier Corporation.

TAM, D., VON ARNIM, V., MCKINLEY, G. H. & HOSOI, A. E. 2009 Marangoni convection in droplets on superhydrophobic surfaces. *J. Fluid Mech.* **624**, 101–123.

https://doi.org/10.1017/jfm.2019.373 Published online by Cambridge University Press

VARANAKKOTTU, S. N., ANYFANTAKIS, M., MOREL, M., RUDIUK, S. & BAIGL, D. 2015 Light-directed particle patterning by evaporative optical Marangoni assembly. *Nano Lett.* **16** (1), 644–650.

VOGEL, N., RETSCH, M., FUSTIN, C-A., DEL CAMPO, A. & JONAS, U. 2015 Advances in colloidal assembly: the design of structure and hierarchy in two and three dimensions. *Chem. Rev.* **115** (13), 6265–6311.

ZENG, D., LATHAM, W. P. & KAR, A. 2006 Shaping of annular laser intensity profiles and their thermal effects for optical trepanning. *Opt. Engng* **45** (1), 014301.

ZHANG, X., ZHANG, J., ZHU, D., LI, X., ZHANG, X., WANG, T. & YANG, B. 2010 A universal approach to fabricate ordered colloidal crystals arrays based on electrostatic self-assembly. *Langmuir* **26** (23), 17936–17942.

https://doi.org/10.1017/jfm.2019.373 Published online by Cambridge University Press